JOURNAL OF AIRCRAFT
Vol. 44, No. 1, January–February 2007

# Modelization and Kinematics Optimization for a Flapping-Wing Microair Vehicle

Thomas Rakotomamonjy*
*Office National d'Études et de Recherches Aérospatiales, 13661 Salon de Provence, France*
Mustapha Ouladsine†
*Laboratoire des Sciences de l'Information et des Systèmes, 13397 Marseille, France*
and
Thierry Le Moing*
*Office National d'Études et de Recherches Aérospatiales, 31055 Toulouse, France*

DOI: 10.2514/1.22960

**OSCAB, a flight-dynamics-oriented simulation model of a flapping-wing microair vehicle, is presented here. This concept is based on flapping flight performed in nature by insects or hummingbirds. The model features two independent wings and integrates the aerodynamic forces computed along each wing to determine the global motion of the microair vehicle with respect to an inertial reference frame. A comparison between our simulation model and previous experimental measurements is presented, showing that it can reproduce the influence of the wing rotation phasing on the total lift. An optimization of the flapping kinematics of the wing has also been conducted to maximize the mean lift. A neural network has been designed to reproduce various function shapes modeling the wing movements. The parameters of this network have been optimized with a genetic algorithm to avoid local extrema. Results show a lift gain from 30 to 40%, corroborating previous experiments.**

## Nomenclature

| | | |
|---|---|---|
| $\boldsymbol{B}_{jk}$ | = | rotation matrix from $\Re_k$ to $\Re_j$ |
| $b$ | = | wing-element width |
| $C$ | = | wing root point |
| $C_x$, $C_z$ | = | drag and lift coefficients |
| $c$ | = | chord |
| $D$ | = | drag |
| $F$ | = | aerodynamic center |
| $\boldsymbol{F}$ | = | force |
| $f$ | = | flapping frequency |
| $G$ | = | mass center of the MAV body |
| $I_G$ | = | inertial tensor in $G$ |
| $i$ | = | current wing element, $1 \leq i \leq n$ |
| $L$ | = | lift |
| $l$ | = | distance between the leading edge and the rotation axis |
| $\boldsymbol{M}$ | = | moment |
| $m$ | = | mass |
| $n$ | = | total number of wing elements |
| $O$ | = | geometrical center of the MAV body |
| $p$, $q$, $r$ | = | roll, pitch, and yaw rates |
| $\Re_b$ | = | MAV main body frame |
| $\Re_n$ | = | ground frame |
| $\Re_w$ | = | wing frame |
| $S_{\text{ref}}$ | = | reference surface |
| $\boldsymbol{u}$ | = | input vector |
| $u$, $v$, $w$ | = | horizontal, lateral, and vertical translation speeds |
| $\boldsymbol{V}_{P/\Re_j}$ | = | velocity of $P$ with respect to $\Re_j$ |
| $\boldsymbol{v}$ | = | aerodynamic speed |
| $\boldsymbol{x}$ | = | state vector |
| $x_C$, $y_C$, $z_C$ | = | coordinates of $C$ within $\Re_b$ |
| $x_F$, $y_F$, $z_F$ | = | coordinates of $F$ within $\Re_w$ |
| $x_G$, $y_G$, $z_G$ | = | coordinates of $G$ within $\Re_b$ |
| $\alpha$ | = | aerodynamic angle of attack |
| $\Gamma$ | = | aerodynamic circulation |
| $\lambda$ | = | wing flapping angle |
| $\nu$ | = | wing rotation angle |
| $\xi$ | = | stroke plane angle |
| $\rho$ | = | air density |
| $\phi$, $\theta$, $\psi$ | = | roll, pitch, and yaw angles |
| $\boldsymbol{\Omega}_{jk}$ | = | rotation vector between $\Re_k$ and $\Re_j$ |

*Subscripts*

| | | |
|---|---|---|
| $l$, $r$ | = | respectively, left or right wing |
| 1, 2, 3 | = | vector components |

*Superscripts*

| | | |
|---|---|---|
| mas | = | added mass component |
| rot | = | rotational circulation component |
| st | = | steady aerodynamic component |

## Introduction

BECAUSE they are becoming of great interest in both civil and military applications, microair vehicles (MAVs) represent a large field of investigation. Civilian applications include the monitoring of forest fires, inspecting high monuments, and interventions in narrow and hazardous environments, where it would be too dangerous to send a human agent. MAVs could also be used for military purposes by being able to be carried by a single infantryman, and to operate autonomously for observation and "behind the hill" reconnaissance missions.

Current prototypes focus mainly on fixed-wing (plane-type) or rotary-wing (helicopter-type) designs. Instead, a flapping-wing model is presented here. This concept is based on natural flight performed by insects or hummingbirds. Although the flapping-wing motion involves more complex mechanisms, it offers certain advantages in comparison with the fixed and rotary-wing MAVs. First, it is easy to see that fixed-wing MAVs, just like classical aircraft, cannot fly below certain longitudinal speed to keep them

Received 6 February 2006; revision received 6 July 2006; accepted for publication 9 July 2006. 

*Research Engineer, Systems Control and Flight Dynamics Department, Base aérienne 701.

†Professor, Control and Simulation team, Domaine Universitaire de Saint-Jérôme.

airborne. Nature offers the example of insects or hummingbirds hovering above flowers or maneuvering at low speeds with precision for feeding or gathering pollen. Rotary-wing MAVs can perform low-speed flight, but their main drawback is that their acoustical spectrum is centered around one single frequency (the rotor rotation frequency). Flapping-wing flight offers a more spread spectrum, ensuring more discretion for the military purposes.

The work presented here is conducted in parallel with the *Projet de Recherches Fédérateur* (federative research project, hereafter PRF) REMANTA at the ONERA [1]. It aims to enlarge the scientific or technical knowledge and methods in the field of flapping wings MAVs.

A bibliographic study of the available papers on natural flapping flight and its applications to artificial aerial devices shows two possible configurations for this type of flight:

1) Bird-like flight, in which the wings flap at low/medium frequency within a near vertical plane. Both lift and thrust are generated during the downstroke, and the articulated wings fold back during the upstroke so as not to produce negative lift. Most large birds can also keep their wings spread to stay aloft, but this mechanism could be considered more as gliding than flying.

2) Insect-like flight, where the wings flap at a higher frequency within a horizontal or slightly inclined plane, generating lift in both strokes directions (back and forth). This last kind of flapping flight is also typical of the hummingbird, who is the only bird that masters hovering flight.

Many authors have worked on understanding the animal flight during the last century. The main obstacle was the inability of the classical aerodynamic mechanisms known by then to explain the insect flight. The application of classical theorems to a pair of insect wings gave a too small lift to sustain the flying animal, a problem summarized as the famous paradox *bumblebees cannot fly*. Weis-Fogh was one of the first to propose the existence of unstationary aerodynamic mechanisms thanks to the observation of various species of flying insects as well as an evaluation of the power required for hovering [2,3]. In particular, he suggested that the quick clapping and peeling of the wings accelerated the establishment of the aerodynamical circulation around the wings and enhanced the lift.

Ellington [4] also wrote a very detailed analysis of hovering flight of insects, detailing the different types of wing kinematics according to the species, and gathering a large amount of data on insect morphology. Żbikowski [5] discussed various analytical models for the aerodynamic effects involved in hovering flight, whereas many studies relied on a global approach to calculate the produced lift and drag; see, for example, the works of Norberg [6]. She proposed a model inspired by the Rankine–Froude momentum theory to calculate the lift of a hovering bat, and she compared the estimated required power to stay aloft with energy measurements on real bats.

Experimental results were given by Dickinson et al. [7], who reproduced the flow around a fly wing (*Drosophila melanogaster*) using a scaled-wing model flapping in mineral oil to keep the Reynolds similitude ($Re \approx 10^3$–$10^4$ for insect flight). Three specific aerodynamic effects have been shown as the cause of a lift gain at low Reynolds number: the circulation generated by the rotation of the wing at the end of a stroke, the delayed stall due to the instationarity of the movement, and finally the wake capture, as the wing reenters the flow it has previously disturbed.

## Presentation of the Simulation Model OSCAB

A simulation model, called OSCAB (which stands for *Outil de Simulation de Concept d'Ailes Battantes*, French for "flapping-wing concept simulation tool"), has been initially written by T. Le Moing (ONERA) in C + + object language [8]. It computes at each time step the values of the internal variables such as velocities, forces, and momentums as a function of the controllable inputs. There are three independent inputs for each wing, corresponding to the three possible rotations of the wing with respect to the body: $\xi$ is the angle of the stroke plane ($\xi = 0$ when the wing flaps vertically and $\xi = \pi/2$ when it flaps horizontally), $\lambda$ is the angle locating the wing within the stroke plane, and $\nu$ is the angle of rotation of the wing around its longitudinal axis. Those angles are represented in Fig. 2. Each wing can move independently, so we have in the most general case a total of 6 inputs:

$$\boldsymbol{u} = {}^t(\xi_l \xi_r \lambda_l \lambda_r \nu_l \nu_r) \tag{1}$$

We have chosen a local-type approach for our model, dividing the wing along its span axis in $n$ rectangular slices according to 2-D approach. The wing kinematics and the global motion of the MAV allow us to compute the local aerodynamic velocities for each wing element. This defines a local aerodynamic frame, and thus a corresponding aerodynamic angle of attack. The elemental forces are then calculated, according to the analytical models adopted to represent the different components of the aerodynamic force, and those forces are summed along the wing, giving a global force and moment applied to the mass center of the MAV.

Although such a local bidimensional approach does not take account for the transversal components of the flow, it has been stated that it was sufficient to reproduce the commonly observed phenomena for this case of flight, and furthermore that flight-dynamics-oriented problems, such as simulation and control, could be more easily treated than with the CFD-based methods [9]. Finally, the total dynamic components (forces and moments) are integrated within an inertial frame to give, according to Newton's first law (NL), the kinematic components of the MAV: three translational velocities $u$, $v$, $w$ along each axis of the earth-bound inertial frame and three rotational velocities $p$, $q$, $r$ (respectively, roll, pitch, and yaw). An overview of the structure of this model is given in Fig. 1.

### Local Aerodynamic Angle of Attack

Respectively, let $\Re_n$, $\Re_b$, $\Re_w$ be the frames attached to the ground, the body of the MAV, and a given wing. We suppose first that the surrounding air in which flies our MAV is immobile with respect to the ground frame $\Re_n$:

$$\boldsymbol{V}_{\text{air}/\Re_n} = \boldsymbol{0} \tag{2a}$$

$$\Leftrightarrow \boldsymbol{V}_{\text{air}/F(i)} + \boldsymbol{V}_{F(i)/\Re_n} = \boldsymbol{0} \tag{2b}$$

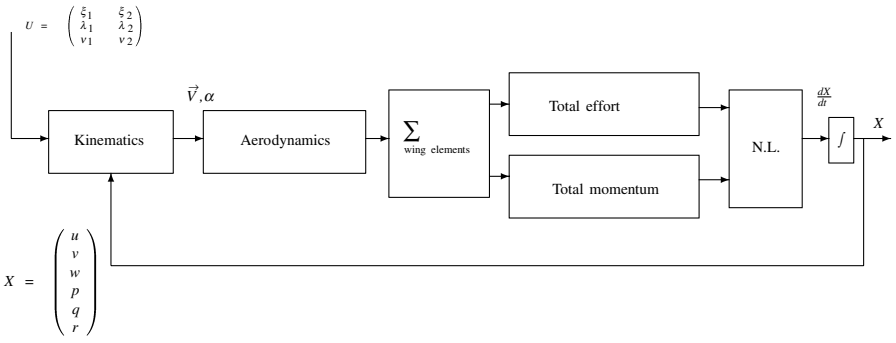


**Fig. 1 Structure of the simulation model.**

$F(i)$ being the aerodynamic center of the $i$th wing element. Calling $P$ a fixed point the Galilean frame $\mathcal{R}_0$, $G$ the mass center of the MAV, and $C$ the junction point between the wing and the body, the aerodynamic velocity $\boldsymbol{v}(i)$ on the considered wing element can be written as

$$\boldsymbol{v}\,(i) \triangleq \boldsymbol{V}_{\text{air}/F(i)} = -\boldsymbol{V}_{F(i)/\Re_n} \tag{3a}$$

$$= -\frac{\mathrm{d}}{\mathrm{d}t/\mathcal{R}_0}(\boldsymbol{PF}_i) \tag{3b}$$

$$= -\frac{\mathrm{d}}{\mathrm{d}t/\mathcal{R}_0}(\boldsymbol{PO}) - \frac{\mathrm{d}}{\mathrm{d}t/\mathcal{R}_0}(\boldsymbol{OC}) - \frac{\mathrm{d}}{\mathrm{d}t/\mathcal{R}_0}[\boldsymbol{CF}(i)] \tag{3c}$$

which gives, after reduction [10]

$$\boldsymbol{v}\,(i) = -\boldsymbol{V}_O - \boldsymbol{\Omega}_{nb} \wedge \boldsymbol{OC} - \boldsymbol{\Omega}_{bw} \wedge \boldsymbol{CF}(i) - \boldsymbol{\Omega}_{nb} \wedge \boldsymbol{CF}(i) \tag{4}$$

where $\boldsymbol{V}_O = \boldsymbol{V}_{O/\Re_n}$ is the global velocity of the MAV. By expressing each vector in its reference frame, we get

$$\boldsymbol{v} = -\boldsymbol{B}_{wn} \cdot \begin{pmatrix} u \\ v \\ w \end{pmatrix} - \boldsymbol{B}_{wb} \cdot \begin{pmatrix} p \\ q \\ r \end{pmatrix} \wedge \left[ \boldsymbol{B}_{wb} \cdot \begin{pmatrix} x_C \\ y_C \\ z_C \end{pmatrix} + \begin{pmatrix} x_F \\ y_F \\ 0 \end{pmatrix} \right] - \boldsymbol{\Omega}_{bw} \wedge \begin{pmatrix} x_F \\ y_F \\ 0 \end{pmatrix} \tag{5}$$

with

$$\boldsymbol{B}_{wb} = \begin{pmatrix} \cos\xi\cos\nu - \sin\xi\cos\lambda\sin\nu & \sin\lambda\sin\nu & -\sin\xi\cos\nu - \cos\xi\cos\lambda\sin\nu \\ \sin\xi\sin\lambda & \cos\lambda & \cos\xi\sin\lambda \\ \cos\xi\sin\nu + \sin\xi\cos\lambda\cos\nu & -\sin\lambda\cos\nu & -\sin\xi\sin\nu + \cos\xi\cos\lambda\cos\nu \end{pmatrix} \tag{6}$$

$$\boldsymbol{B}_{nb} = \begin{pmatrix} \cos\psi\cos\theta & \cos\psi\sin\theta\sin\phi - \sin\psi\cos\phi & \cos\psi\sin\theta\cos\phi + \sin\psi\sin\phi \\ \sin\psi\cos\theta & \sin\psi\sin\theta\sin\phi + \cos\psi\cos\phi & \sin\psi\sin\theta\cos\phi - \cos\psi\sin\phi \\ -\sin\theta & \cos\theta\sin\phi & \cos\theta\cos\phi \end{pmatrix} \tag{7}$$

$$\boldsymbol{B}_{wn} = \boldsymbol{B}_{wb} \cdot {}^{t}\boldsymbol{B}_{nb} \tag{8}$$

$$\boldsymbol{\Omega}_{bw} = \begin{pmatrix} \dot{\lambda}\cos\nu \\ 0 \\ \dot{\lambda}\sin\nu \end{pmatrix} \tag{9}$$

The local aerodynamic angle of attack $\alpha_i$ can finally be calculated:

$$\alpha(i) = \angle[-\boldsymbol{v}_1(i) - \mathbf{i} \cdot \boldsymbol{v}_3(i)] \qquad (\mathbf{i}^2 = -1) \tag{10}$$

**Aerodynamic Forces**

For a given wing element, the two components (drag and lift) of the stationary aerodynamic forces can be modeled within the aerodynamic frame as

$$D^{\text{st}} = -\frac{1}{2}\rho S_{\text{ref}} \boldsymbol{v}^2 C_x(\alpha) \tag{11}$$

$$L^{\text{st}} = -\frac{1}{2}\rho S_{\text{ref}} \boldsymbol{v}^2 C_z(\alpha) \tag{12}$$

The aerodynamic coefficient functions $C_x$ and $C_z$ are derived from experimental data obtained by Dickinson et al. [7,11].

The low-Reynolds number specific force components are also taken into account. The quick rotation of the wing around its main axis when a stroke ends brings about a circulation of the air in the opposite direction, which increases the lift (*rotational circulation*). The chosen model expresses this circulation as [7,12,13]

$$\Gamma^{\text{rot}} = \pi \dot{\nu} c^2 \left( \frac{3}{4} - \frac{l}{c} \right) \tag{13}$$

where $c$ is the local chord and $l$ the distance between the leading edge and the rotation axis (see Fig. 2 for a better look at the different angles).

Another part of these unstationary aerodynamic forces is the added mass effect, due to the reaction induced by the acceleration of the fluid mass surrounding the wing. This effect, restricted to translation motion, can be written as [13,14]

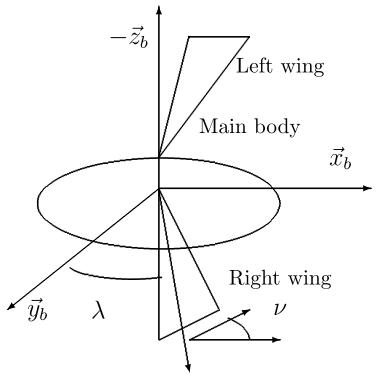


**Fig. 2 Definition of the position angles (for $\xi = \pi/2$).**

$$\Gamma^{\text{mas}} = \frac{\pi}{4} c^2 y_F \frac{1}{|\boldsymbol{v}|} \ddot{\lambda} \tag{14}$$

where $\lambda$ is the angle locating the wing within the stroke plane and $y_F$ is the spanwise coordinate of the aerodynamic center (as the application point of the aerodynamic forces) of the wing element. For both cases, the resulting elemental force is supposed to act normally to the wing chord, and is obtained from the corresponding circulation via

$$L^{\text{rot,mas}} = \rho |\boldsymbol{v}| b \Gamma^{\text{rot,mas}} \tag{15}$$

where $b$ is the width of the considered wing element.

#### Forces and Moments

By addition of these elemental forces expressed within the wing frame, the dynamic resultant $\boldsymbol{R}$ and moment of the aerodynamic forces applied to a given wing can be obtained:

$$\boldsymbol{R}_{l,r} = \sum_{i=1}^{n} \boldsymbol{R}_{l,r}(i) \tag{16}$$

$$\boldsymbol{M}_{l,r} = \sum_{i=1}^{n} \boldsymbol{GF}(i) \wedge \boldsymbol{R}_{l,r}(i) \tag{17}$$

with

$$\boldsymbol{R}_{l,r}(i) = \begin{pmatrix} \cos\alpha(i) & -\sin\alpha(i) \\ \sin\alpha(i) & \cos\alpha(i) \end{pmatrix} \cdot \begin{pmatrix} D^{\text{st}}(i) \\ L^{\text{st}}(i) + L^{\text{rot}}(i) + L^{\text{mas}}(i) \end{pmatrix} \tag{18}$$

Assuming that the only forces applied to the MAV are the aerodynamic ones and its own weight, and by supposing moreover that the mass of each wing can be neglected, the total resultant and moment are, respectively, equal to

$$\boldsymbol{R} = m\boldsymbol{g} + \boldsymbol{B}_{nw_l} \cdot \boldsymbol{R}_l + \boldsymbol{B}_{nw_r} \cdot \boldsymbol{R}_r \tag{19}$$

$$\boldsymbol{M} = \boldsymbol{B}_{nw_l} \cdot \boldsymbol{M}_l + \boldsymbol{B}_{nw_r} \cdot \boldsymbol{M}_r \tag{20}$$

where $\boldsymbol{g}$ is the gravitational acceleration. Newton's second law finally leads to the global translation and rotation velocities, by integration of [10]

$$\boldsymbol{R} = m \frac{\mathrm{d}}{\mathrm{d}t/\mathcal{R}_n} (\boldsymbol{V}_{G/\Re_n}) \tag{21}$$

$$\boldsymbol{V}_{O/\Re_n} = \boldsymbol{V}_{G/\Re_n} + \boldsymbol{OG} \wedge \boldsymbol{\Omega}_{bn} \tag{22}$$

and

$$\boldsymbol{M} = \frac{\mathrm{d}}{\mathrm{d}t/\mathcal{R}_n} (\boldsymbol{I}_G \cdot \boldsymbol{\Omega}_{bn}) \tag{23a}$$

$$= \boldsymbol{I}_G \cdot \frac{\mathrm{d}}{\mathrm{d}t/\mathcal{R}_n} (\boldsymbol{\Omega}_{bn}) + \boldsymbol{\Omega}_{bn} \wedge \boldsymbol{I}_G \cdot \boldsymbol{\Omega}_{bn} \tag{23b}$$

$$= \boldsymbol{I}_G \cdot \begin{pmatrix} \dot{p} \\ \dot{q} \\ \dot{r} \end{pmatrix} + \begin{pmatrix} p \\ q \\ r \end{pmatrix} \wedge \boldsymbol{I}_G \cdot \begin{pmatrix} p \\ q \\ r \end{pmatrix} \tag{23c}$$

where $\boldsymbol{I}_G$ is the inertial tensor of the body expressed in $G$.

## Validation of the Simulation Model

To prove the reliability of this simulation model, a comparison has been made with the experimental results obtained by Dickinson et al. [7] with the *Robofly* experiment. In particular, it has been shown that the timing of the wing rotation with respect to the flapping has a strong influence upon the total lift: if the rotation of the wing begins slightly before the end of the stroke (*advanced* phase rotation), some extra lift is generated, which is clearly visible as a peak on the vertical force records; see Fig. 3. On the contrary, if this rotation occurs after

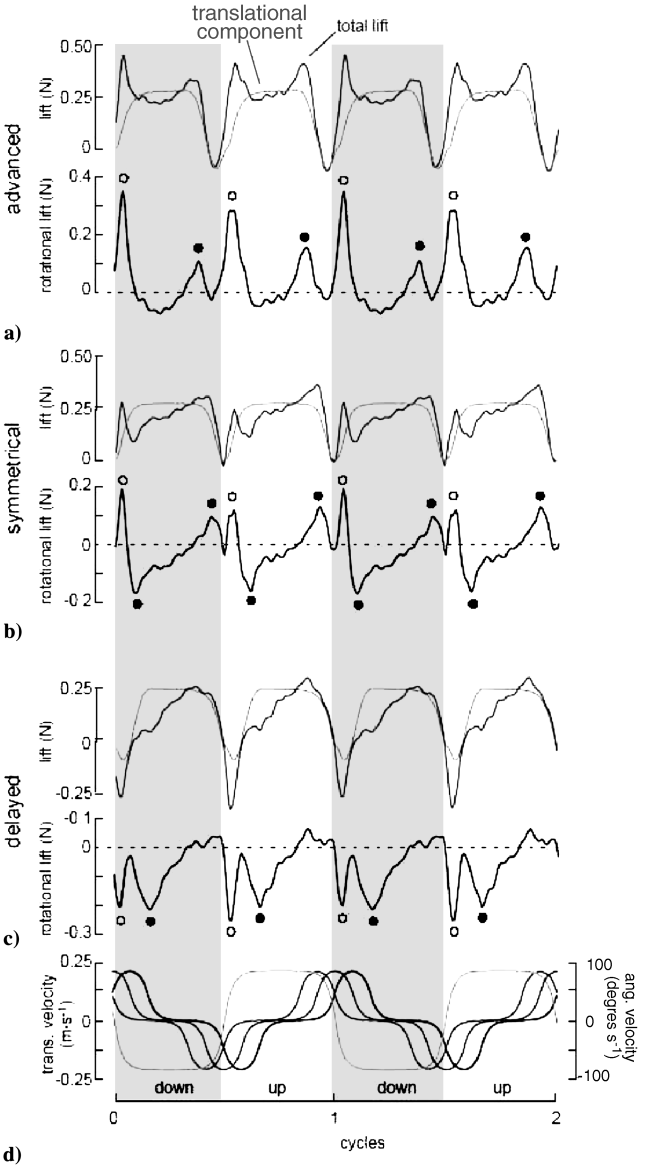


**Fig. 3 Effect of wing rotation upon lift, after Dickinson et al. [7].**

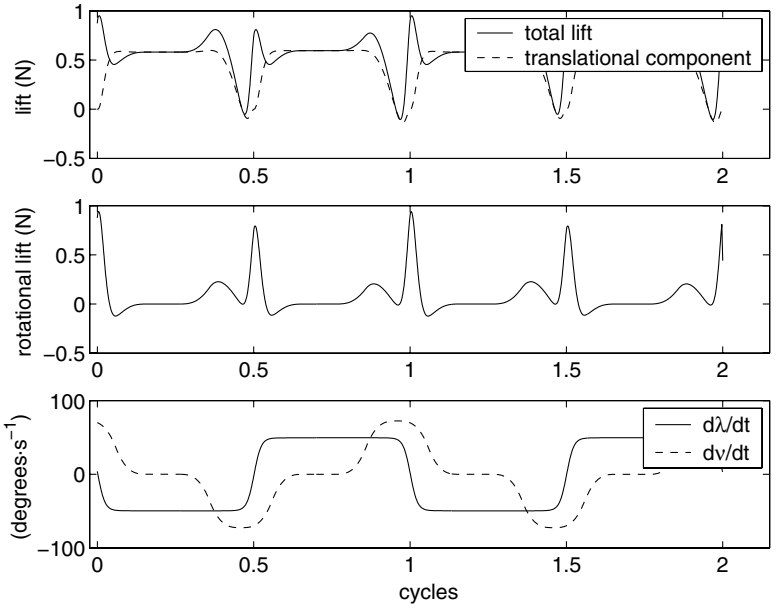


**Fig. 4 Effect of wing rotation upon lift, $\Delta\Phi = +15$ deg, OSCAB simulation.**

the beginning of the reverse stroke (*delayed* phase rotation), it induces a loss of lift.

The wing kinematics of this experiment have been reproduced with the OSCAB simulation model, using a similar configuration: the flapping frequency is $f = 0.145$ Hz, the total wing length is 25 cm, and the density of the surrounding fluid is $\rho = 0.88e\text{-}3$ kg $\cdot$ m$^{-3}$. The inputs $\lambda$ and $\nu$ are, respectively, modeled with a triangular-shaped signal (which corresponds to a constant angular velocity during each stroke), and a square-shaped signal, to ensure a constant angle of attack within a stroke. The aforementioned functions are equal to

$$\lambda(t) = \lambda_0 \int_0^t \tanh[k_\lambda \cos(\omega u)]\,\mathrm{d}u \tag{24}$$

$$\nu(t) = \nu_0 \tanh[k_\nu \cos(\omega t + \Delta\Phi)] \tag{25}$$

$k_\lambda$ and $k_\nu$ being parameters influencing the slope of the front and back edges of the signal. The phase difference between $\lambda$ and $\nu$ for advanced/delayed rotation is $\Delta\Phi = \pm 15$ deg.

The simulation results are presented in Figs. 4–6. It is very interesting to notice how they match the experimental ones: a phase advance and a phase delay of $\nu$ with respect to $\lambda$ cause, respectively, a gain and a loss of lift in comparison to the nominal settings, which proves that this model is able to reproduce a correct influence of the wing kinematics over the global aerodynamic forces. We can already think about a differential control of the phase of the rotation of each wing, which would generate a different lift between the wings and thus a roll momentum, a strategy that some authors think is already used by real insects to quickly change direction [15].

Another series of comparisons was made, this time with respect to CFD results obtained by Kurtulus et al. [16]. The unsteady, incompressible, 2-D, laminar Navier–Stokes flow equations were numerically solved for a wing performing a back-and-forth motion in a horizontal plane with a symmetrical rotation at the end of each stroke, with a Reynolds number equal to 1000. Among other quantities, the average global lift coefficient was computed for different values of the geometrical angle of attack and of $x_a/c$, $x_a$ being defined as the wing position along the translation axis at the beginning of the rotation. We adopted a similar configuration in

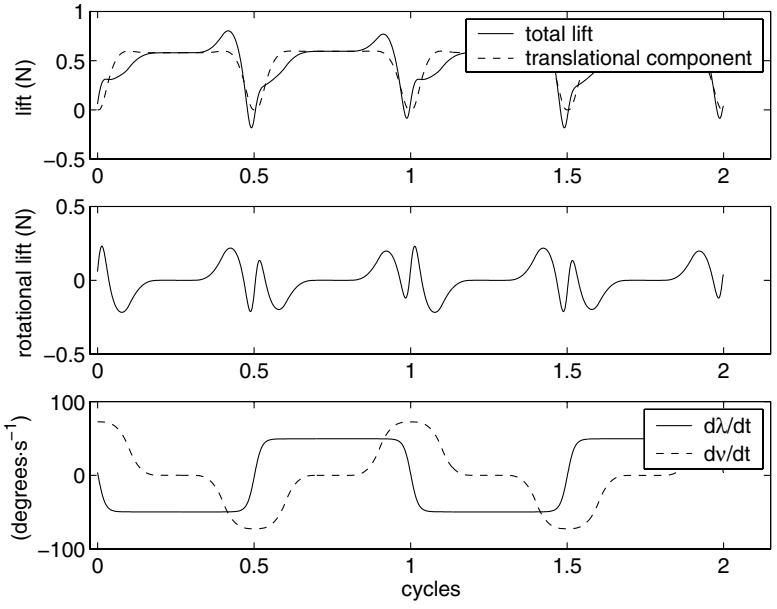


**Fig. 5 Effect of wing rotation upon lift, $\Delta\Phi = 0$ deg, OSCAB simulation.**

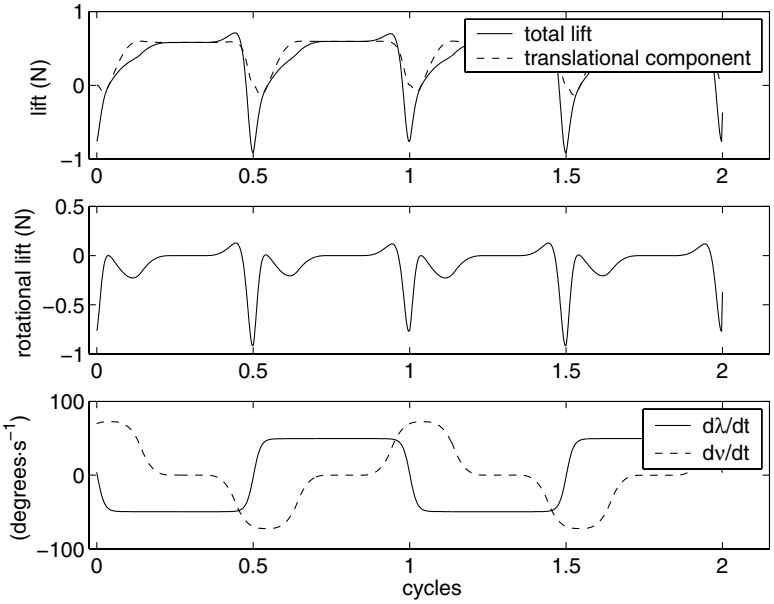


**Fig. 6 Effect of wing rotation upon lift, $\Delta\Phi = -15$ deg, OSCAB simulation.**

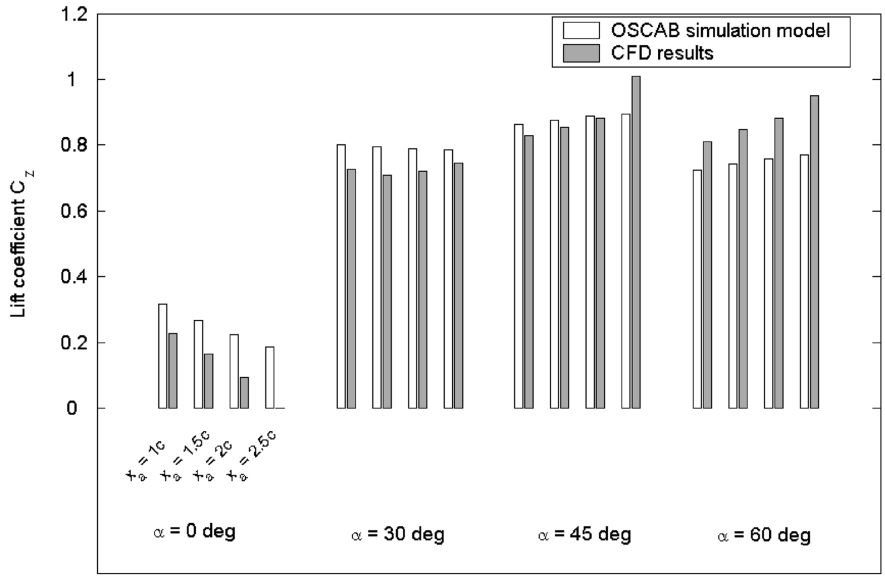


**Fig. 7 Comparison with CFD results for various wing kinematics.**

OSCAB, and the compared results are shown in Fig. 7. Here again, both results are quite similar, indicating that our model offers a good comprehension of the aerodynamics of flapping flight. The small differences could be due to the fact that the wing motion as computed by the CFD method is a pure translation, whereas OSCAB defines the flapping motion as resulting from a rotation of the wing span axis around a fixed point of the body (as depicted in Fig. 2).

It appears though that this model remains highly complex and difficult to express as a simple analytical transfer between inputs and outputs, in particular because it shows many matrix products to convert vector coordinates from one frame to another one. This is why a simpler version of this model has been written [17], to facilitate interpretation as well as to allow later use of classical tools for stabilization and control.

## Simplified Longitudinal Model

### Description

The hypotheses made to derive the simplified model concern mainly the flight domain. We suppose first that the MAV movements are confined in a vertical plane, which serves also as a symmetry plane for the wings and body movements; there is neither roll nor yaw movements, but only pitch:

$$\nu \equiv p \equiv r \equiv 0 \tag{26}$$

These restrictions are more commonly called *longitudinal flight* in flight mechanics.

Another major simplification is neglecting in the computations the translation speeds of the body within the ground frame $\mathcal{R}_0$ in comparison with the aerodynamic speeds on the wing:

$$u, w \ll \dot{\lambda} b \tag{27}$$

This hypothesis is well suited to the cases where the wings flap with a high frequency (e.g., for insects or hummingbirds) and for low-speed flight (approach for example), a fortiori for hovering.

Finally, each wing contains only one slice: $n = 1$ and flapping occurs in a horizontal plane, also similarly to hummingbirds and to some insects: $\xi = \pi/2$.

The number of inputs can then be reduced from 6 ($2 \times 3$ per wing for the complete model) to 2: $\lambda$ and $\nu$. Under these hypotheses, a relation has been derived between the state vector $\boldsymbol{x}$, reduced here to $\boldsymbol{x} = {}^t(uwq)$, and the input vector $\boldsymbol{u} = {}^t(\lambda \nu \dot{\lambda}\ \dot{\nu}\ \ddot{\lambda})$:

$$\dot{\boldsymbol{x}} = J(\boldsymbol{u}) \cdot F(\boldsymbol{x}, \boldsymbol{u}) + C_g \tag{28}$$

with

$$J(\boldsymbol{u}) = \begin{bmatrix} E_1(\boldsymbol{u}) & E_2(\boldsymbol{u}) \\ G_1(\boldsymbol{u}) & G_2(\boldsymbol{u}) \\ H_1(\boldsymbol{u}) & H_2(\boldsymbol{u}) \end{bmatrix} \tag{29}$$

$$F(\boldsymbol{x}, \boldsymbol{u}) = {}^t\begin{bmatrix} F_1(\boldsymbol{x}, \boldsymbol{u}) & F_2(\boldsymbol{x}, \boldsymbol{u}) \end{bmatrix} \tag{30}$$

$$C_g = {}^t\begin{bmatrix} 0 & g & \frac{mgx_G}{I} \end{bmatrix} \tag{31}$$

Functions $E$, $F$, $G$, and $H$ are nonlinear scalar functions of $\boldsymbol{x}$, $\boldsymbol{u}$, and their time derivatives. $C_g$ is a constant representing the effects of gravity, themselves being functions of mass, gravitational acceleration $g$, longitudinal position of the center of mass $x_G$ of the MAV, and the pitch moment of inertia $I$, detailed next:

$$E_1(\boldsymbol{u}) = \frac{1}{m}(\cos \boldsymbol{u}_1 \sin \boldsymbol{u}_2) \tag{32}$$

$$\begin{aligned} &F_1(\boldsymbol{x}, \boldsymbol{u}) \\ &= \frac{\rho(V_{a_x}^2 + V_{a_z}^2)S}{m}\left[k_{C_{t1}} \cos\left(2 \arctan \frac{-V_{a_z}}{-V_{a_x} + \sqrt{V_{a_x}^2 + V_{a_z}^2}}\right)\right. \\ &\left. + k_{C_{t3}} \cos\left(6 \arctan \frac{-V_{a_z}}{-V_{a_x} + \sqrt{V_{a_x}^2 + V_{a_z}^2}}\right)\right] \end{aligned} \tag{33}$$

with

$$V_{a_x} = -(\boldsymbol{x}_3 \sin \boldsymbol{u}_1 \cos \boldsymbol{u}_2 - \boldsymbol{u}_3 \sin \boldsymbol{u}_2) y_F \tag{34}$$

$$V_{a_z} = -(\boldsymbol{x}_3 \sin \boldsymbol{u}_1 \sin \boldsymbol{u}_2 + \boldsymbol{u}_3 \cos \boldsymbol{u}_2) y_F + \boldsymbol{x}_3 \cos \boldsymbol{u}_1 x_F \tag{35}$$

$$\begin{bmatrix} k_{C_{t1}} & k_{C_{t3}} \end{bmatrix} = \begin{bmatrix} 0.27 & 0.10 \end{bmatrix} \tag{36}$$

Similarly we have

$$E_2(\boldsymbol{u}) = -\frac{1}{m}(\cos \boldsymbol{u}_1 \cos \boldsymbol{u}_2) \tag{37}$$

$$\begin{aligned} &F_2(\boldsymbol{x}, \boldsymbol{u}) \\ &= \frac{\rho(V_{a_x}^2 + V_{a_z}^2)S}{m}\left[k_{C_{n1}} \sin\left(2 \arctan \frac{-V_{a_z}}{-V_{a_x} + \sqrt{V_{a_x}^2 + V_{a_z}^2}}\right)\right. \\ &\left. + k_{C_{n3}} \sin\left(6 \arctan \frac{-V_{a_z}}{-V_{a_x} + \sqrt{V_{a_x}^2 + V_{a_z}^2}}\right)\right] \\ &+ \frac{2\pi c \boldsymbol{u}_4}{m\sqrt{V_{a_x}^2 + V_{a_z}^2}}\left(\frac{3}{4} - \hat{x}_0\right) + \frac{\pi c y_F \boldsymbol{u}_5}{2m(V_{a_x}^2 + V_{a_z}^2)} \end{aligned} \tag{38}$$

$$G_1(\boldsymbol{u}) = \frac{1}{m}\cos \boldsymbol{u}_2 \tag{39}$$

$$G_2(\boldsymbol{u}) = \frac{1}{m}\sin \boldsymbol{u}_2 \tag{40}$$

$$H_1(\boldsymbol{u}) = -\frac{1}{I} y_F \sin \boldsymbol{u}_1 \cos \boldsymbol{u}_2 \tag{41}$$

$$H_2(\boldsymbol{u}) = \frac{1}{I}(x_F \cos \boldsymbol{u}_1 - y_F \sin \boldsymbol{u}_1 \sin \boldsymbol{u}_2) \tag{42}$$

$$\begin{bmatrix} k_{C_{n1}} & k_{C_{n3}} \end{bmatrix} = \begin{bmatrix} 3.57 & 0.10 \end{bmatrix} \tag{43}$$

$\{k_{C_{t1}}, k_{C_{t3}}, k_{C_{n1}}, k_{C_{n3}}\}$ are aerodynamical coefficients derived from the chosen model for the aerodynamic stationary forces (11) and (12).

This simplification allows us to give an entirely analytical form of the input/output relation, which was not possible with the complete model, due to the matrix products and the 2-D element decomposition.

#### Validation of the Simplified Model

Because the translation speeds have been neglected in the simplified model, we have to define a validation domain in which this hypothesis is admissible. By considering a standard MAV configuration with a total wingspan of 15 cm flapping at a frequency $f = 40$ Hz, the mean value of the aerodynamic speed can be expressed as

$$\bar{v} = 2\pi \cdot 40 \frac{15e\text{-}3}{4} \approx 9.42 \text{ m} \cdot \text{s}^{-1} \tag{44}$$

By considering that the translation speeds can be neglected as long as they are lower than 1% of the aerodynamic speeds, the maximum translation speed for the preceding hypothesis to remain valid is $100\bar{v} = 9.42$ cm $\cdot$ s$^{-1}$, which is consistent with the hovering or low-speed flight assumption.

For each model, the hovering flapping frequency $f_0$ has been calculated as the frequency for which the mean lift is equal to the weight of the MAV. The evolution of the vertical speed $w$ has then been plotted for frequencies, respectively, equal to $1.2f_0$ and $0.8f_0$. As we can see in Fig. 8, there is little difference between both models: at a flapping frequency above (respectively, below) the hovering frequency, the MAV climbs (respectively, sinks) regularly with a linear growing speed.[‡] By calculating the average acceleration with a linear regression and plotting it for different flapping frequencies, we get a more precise estimation of the domain of validity of the simplified model. In Fig. 9, we can see that both models are very similar for frequencies below 40–45 Hz, which confirms that this simplified model is a valid approximation for low-speed or hovering flight, and could therefore be used to look for stabilization and closed-loop control methods.

## Kinematics Optimization

Because the chosen configuration does not match exactly any living bird or insect, it is not possible to rely on existing wing movement patterns and apply them directly to the simulation model. This is why an optimization of those kinematics has been undertaken to determine the most efficient wing movements [18]. This MAV would have to carry a given payload including sensors, batteries, but also actuators and navigation systems, and it seems logical to consider optimizing the mean lift in hovering flight in a first approach. Because of the periodical nature of the wing movements, the problem has been reduced to one flapping period. Let us note $\bar{L}$, the total mean lift over a period:

$$\bar{L} = \frac{1}{T}\int_0^T R_z(t)\, \mathrm{d}t \tag{45}$$

[‡]The plot is labeled with $-w$ because the vertical axis is downwards-oriented, as it is conventionally done in flight mechanics.

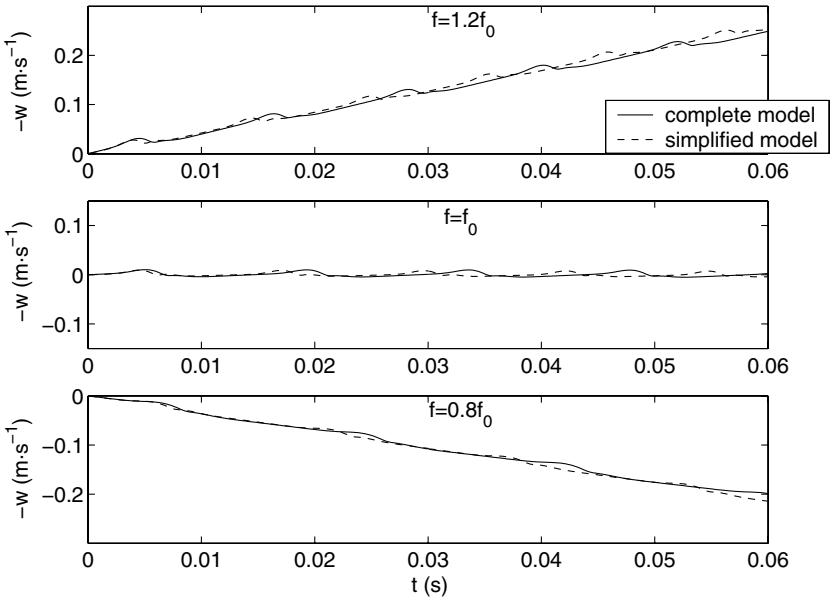


**Fig. 8 Evolution of vertical speed *w*.**

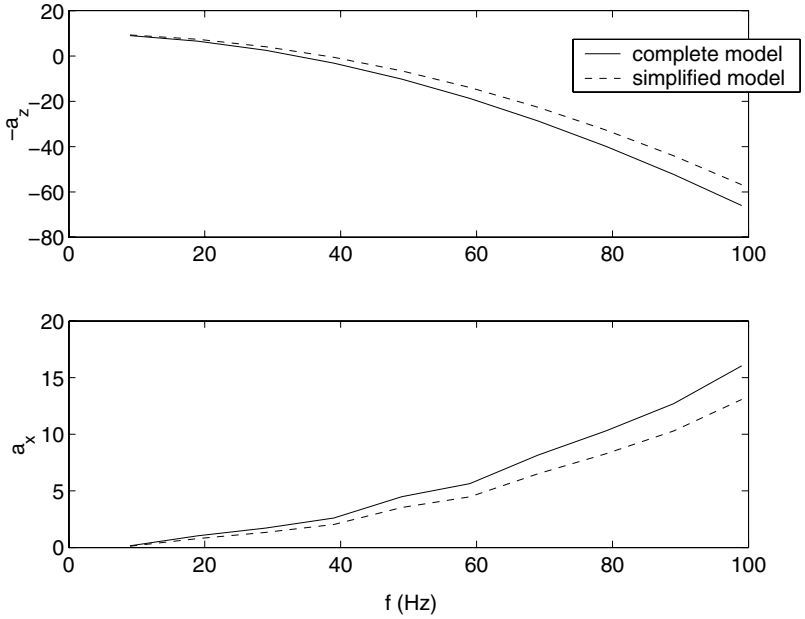


**Fig. 9 Mean acceleration for different flapping frequencies.**

By defining the criterion $J = \bar{L}$, the problem is then to find the kinematics $\lambda(t)$ or $\nu(t)$ which maximize $J$ over a period.

### Input Modeling with Neural Networks

The complexity of the model, mainly due to its nonlinear components, makes it very hard to reach an optimal flapping function expressed as the analytical solution of a functional equation. That is why this potential solution has been modeled under a parametric form, thus transforming a continuous-time optimal control problem into a nonlinear programming problem. But a simple choice of parameters such as amplitude and/or phase means that the global form of the function has to be fixed (triangular, square, etc.). To keep as much variety in the solution functions as possible, the candidate functions were modeled using neural networks, with the idea that a complex enough network could reproduce a large class of admissible functions. The design, initialization, and learning of the network were performed with the *Neural Network* MATLAB® toolbox.

The first step is to choose an adapted network structure. The more complex the network is, the more various signals it can represent, but the optimization will in this case be less efficient, because of the high number of parameters involved. A compromise has to be found to get the minimal network representing as many function shapes as possible suiting the specifications. Observations of natural insect wing kinematics have shown that the geometrical angle of attack remains nearly constant during a stroke, before the wing revolves and begins the next stroke. As a consequence, a square-shaped function

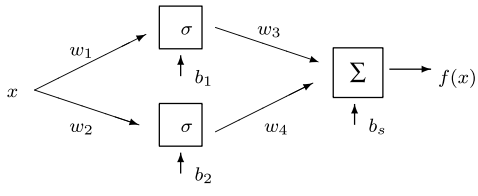


**Fig. 10 Structure of the chosen network.**

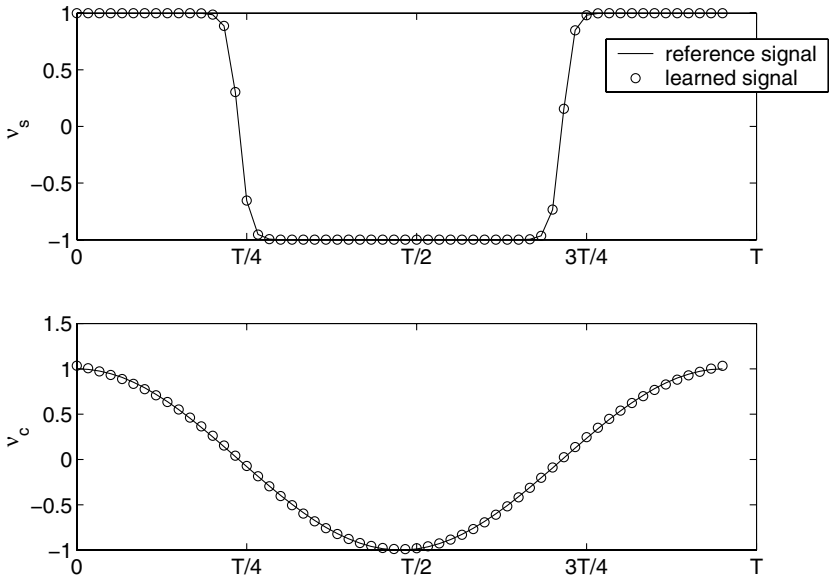


**Fig. 11 Learning of $v_s$ and $v_c$.**

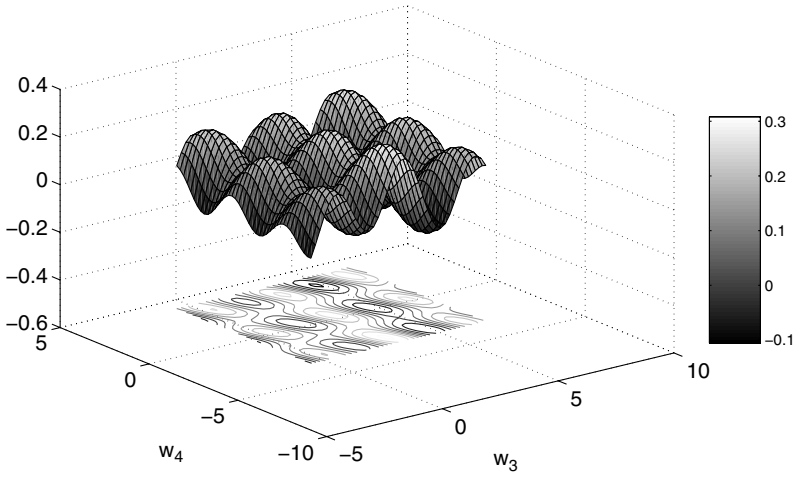


**Fig. 12 Projection of $\bar{L}$ within $(w_3; w_4)$ plane.**

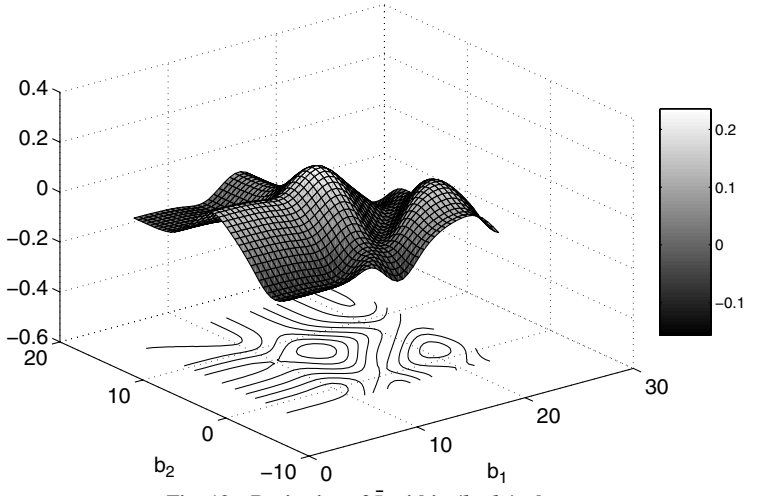


**Fig. 13 Projection of $\bar{L}$ within $(b_1; b_2)$ plane.**

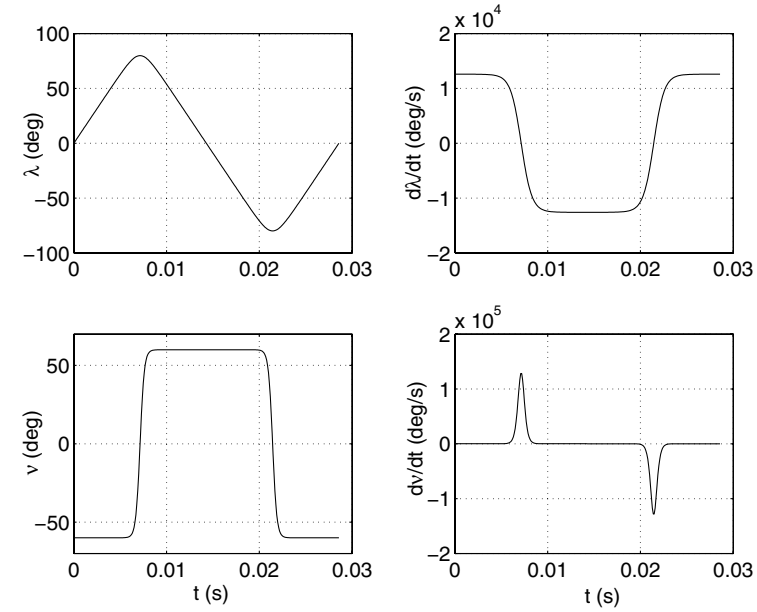


**a) Inputs $\lambda, \nu$**

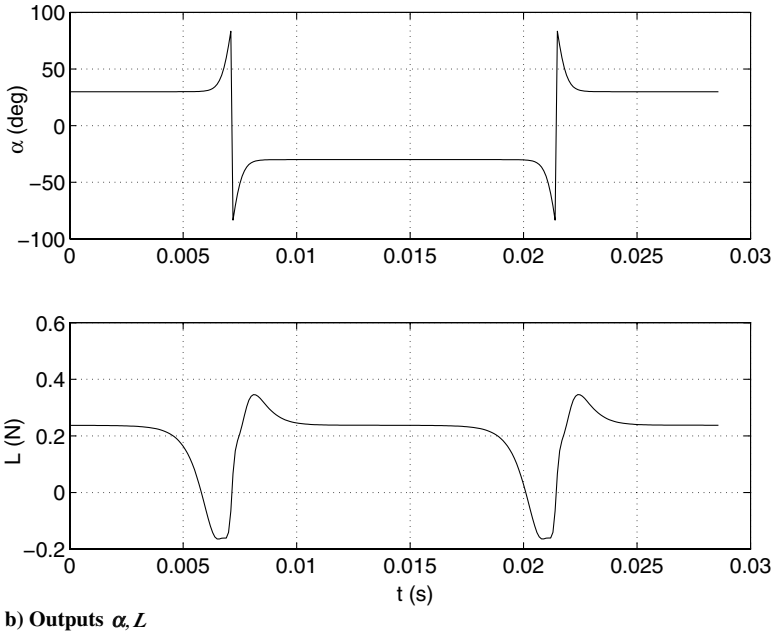


**b) Outputs $\alpha, L$**

**Fig. 14 Reference inputs $\lambda_r$ and $\nu_r$.**

was used as a basis for the rotation angle $\nu(t)$. But we have to consider also more classical functions, such as trigonometric ones, for example: the chosen network must then be able to reproduce square $\nu_s = \tanh(k_r \cos \omega t)$ as well as cosine $\nu_c = \cos \omega t$ functions. After a few searches, we found that the minimal network reproducing both kind of signals features two layers, with two neurons on the hidden layer (input layer) and one neuron on the output layer. This network is shown in Fig. 10. The neurons on the hidden layer have a sigmoid transfer function $\sigma(u) = 1/(1 + e^{-u})$, and the output one a linear transfer (and acts just as a summing element). The weights $\{w_i\}_{i=1\ldots4}$ on each connection plus the biases give a total of $4 + 3 = 7$ parameters to be optimized.

The learning uses the retropropagation method, available in the aforementioned MATLAB® toolbox. The results of learning of $\nu_s$ and $\nu_c$ during one period (given the periodic nature of the model inputs) are shown in Fig. 11.

This network appears able to reproduce those function shapes, as well as some others (which were not represented here) such as trapeze-shaped functions, where the junction between the constant floors are made using sine or polynomial arcs. The same operation is performed to model the flapping angle $\lambda(t)$: this time, a total of four neurons on the hidden layer was necessary to reproduce the largest class of shapes.

#### Optimization algorithm

Let $n$ be the number of neurons on the hidden layer of the network. $\{w_i\}_{i=1\ldots n}$ are the input weights, $\{w_i\}_{i=n\ldots 2n}$ the output weights, $\{b_i\}_{i=1\ldots n}$ the neuron biases, and $b_s$ the output bias. Let also $\Theta = (\{w_i\}_{i=1\ldots 2n}, \{b_i\}_{i=1\ldots n}, b_s)$ be the parameters array subject to optimization, $\hat{\Theta}$ the optimum value, and $f_\Theta(t)$ the corresponding function, which can be directly expressed:

$$f_\Theta(t) = \sum_{i=1}^{n} \frac{w_{i+n}}{1 + e^{-(w_i t + b_i)}} + b_s \tag{46}$$

Standard optimization algorithms (Newton and sequential quadratic programming methods) have been first used to find $\hat{\Theta}$. But the results

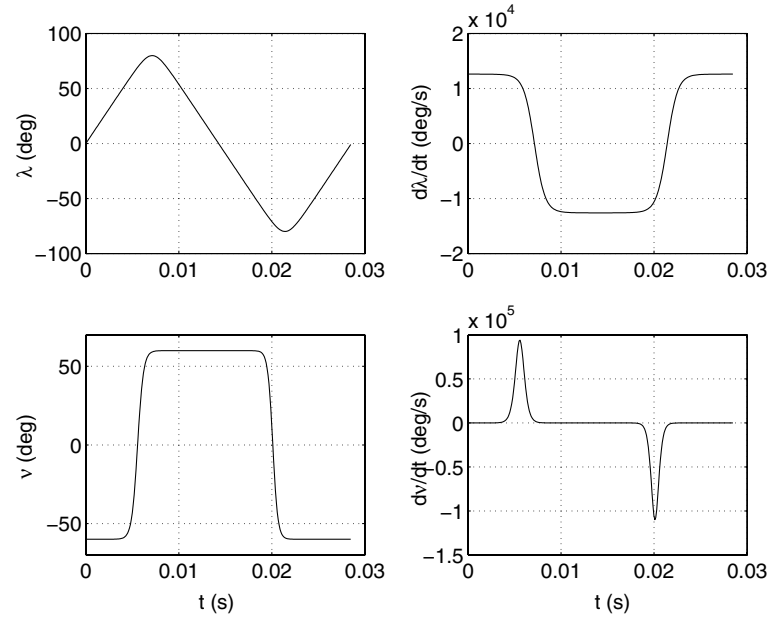


**a) Inputs $\lambda$, $\nu$**

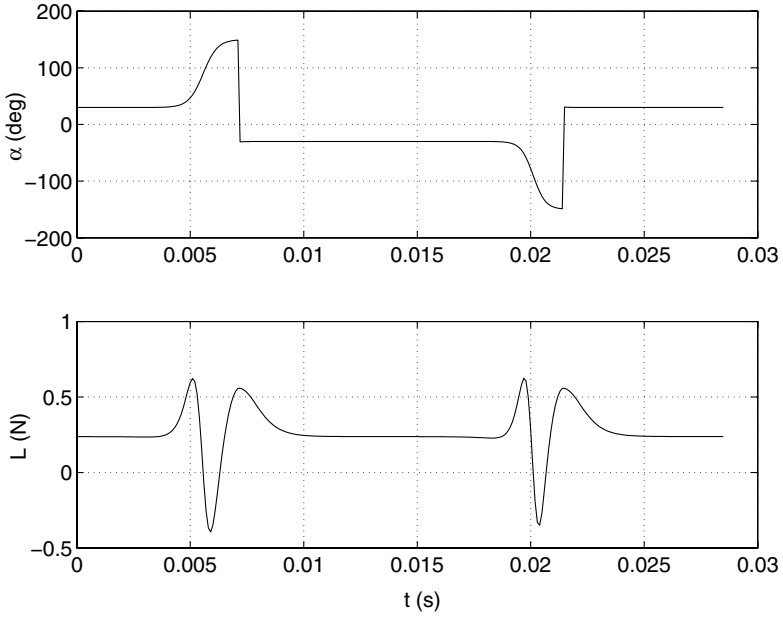


**b) Outputs $\alpha$, $L$**

**Fig. 15 Optimization of rotation angle $\nu$.**

were very dependent upon the initialization point $\Theta_0$, and although the algorithm converged properly, the optimal vector $\hat{\Theta}$ and thus the corresponding kinematics and mean lift were different for many different values of $\Theta_0$. This observation was confirmed by studying the sensitivity of the mean lift over a period $\bar{L}$ with respect to the different components of $\Theta$. Figures 12 and 13 show the values of $\bar{L}$ as a function of $(w_3; w_4)$ and $(b_1; b_2)$, respectively. The undulating shape of the surfaces and the many peaks correspond to local optima, in which a classical optimization algorithm can easily be trapped. That is why a genetic algorithm (GA) was used to try to override those local optima. The principle of this type of algorithm [19] is to generate a population of individuals, each one corresponding to a value of $\Theta$. The population is then mixed, each individual having the ability to recombine his genes (the components of $\Theta$) with a randomly selected other individual to try to find a better candidate to improve $J$.

This algorithm can be summarized as follows:

*Beginning of GA*

initialize population size $N$, maximum number of generations $n_g$ max, conservation factor $G$, mutation factor $M$

for $i = 1$ to $N$ do

$\Theta \leftarrow C_l + \text{rand.}(C_u - C_l)$

$J \leftarrow \bar{L}(\Theta)$

add $\Theta$ to $\mathbf{\Phi}$ {creation of the initial population}

add $J$ to $\mathbf{\Psi}$

end for

$n_g = 1$

$\Psi \leftarrow \{\max(\Psi), \ldots, \min(\Psi)\}$

$\Phi \leftarrow \{\arg[\max(\Psi)], \ldots, \arg[\min(\Psi)]\}$ {sorting of the population according to criterion values}

$\epsilon \leftarrow \Psi(N) - \Psi(1)$

while $\epsilon > \epsilon_{\text{stop}}$ and $n_g < n_g$ max do

$k \leftarrow NG + 1$

while $k \leq N$ do

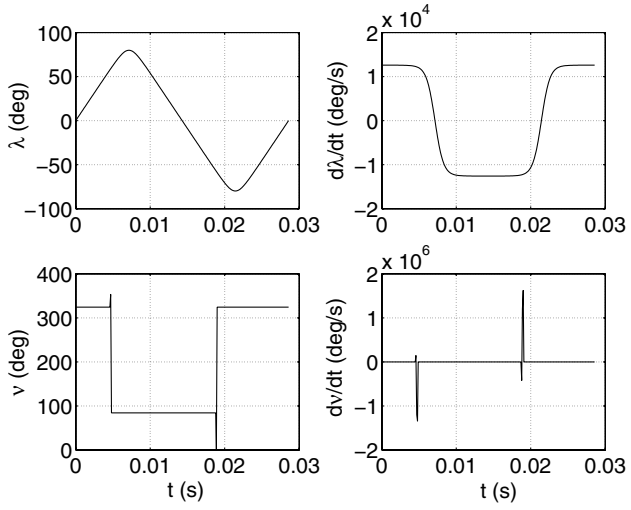


**a) Inputs $\lambda, \nu$**

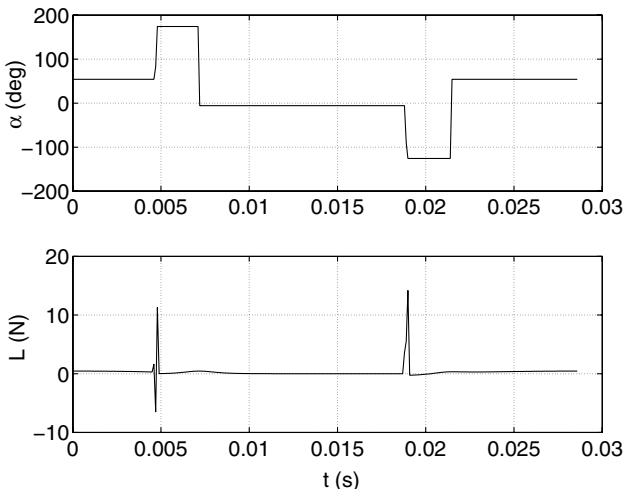


**b) Outputs $\alpha, L$**

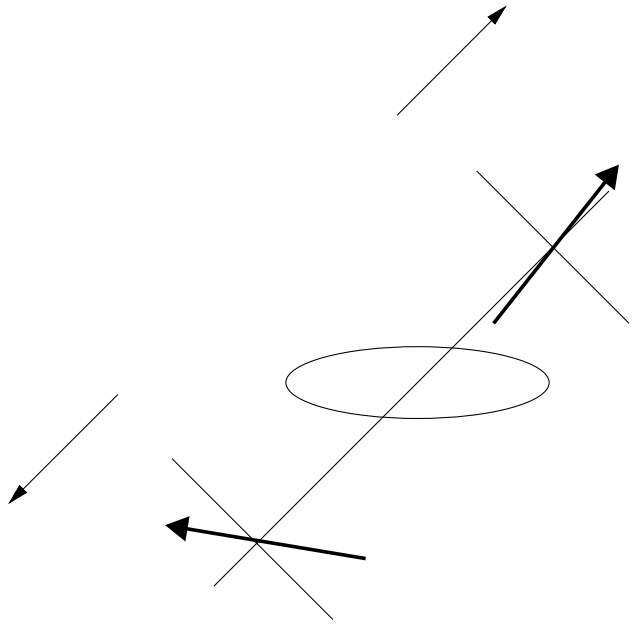

**c) Wing chord motion (arrow=leading edge)**

**Fig. 16 Optimization of $\nu$, $\xi = 45$ deg.**

$k_1, k_2 \leftarrow \text{rand}(NG)$ {random selection of two parents}
$\Phi(k) \leftarrow \Phi(k_1) + \text{rand}.[\Phi(k_2) - \Phi(k_1)]$
$J \leftarrow \bar{L}[\Phi(k)]$
$\tilde{J} \leftarrow \bar{L}[\Phi(NG)]$
if $J \geq \tilde{J}$ {improvement test} then
$k \leftarrow k + 1$
else if rand $\leq M$ then
$\Phi(k) \leftarrow C_l + \text{rand}.(C_u - C_l)$ {random mutation}
$J \leftarrow \bar{L}[\Phi(k)]$
if $J \geq \tilde{J}$ then
$k \leftarrow k + 1$
end if
end if
end while
$\Psi \leftarrow \{\max(\Psi), \ldots, \min(\Psi)\}$
$\Phi \leftarrow \{\arg[\max(\Psi)], \ldots, \arg[\min(\Psi)]\}$
$\epsilon \leftarrow \Psi(N) - \Psi(1)$
$n_g \leftarrow n_g + 1$
end while
$\hat{\Theta} = \Phi(1)$ {optimal individual}
*End of GA*

Because this algorithm does not take any explicit constraint into account, one has to find the way to express the necessity for the optimal solution to be periodic, i.e., $f_{\hat{\Theta}}(0) = f_{\hat{\Theta}}(T)$. This condition is then equivalent to [Eq. (46)]

$$\sum_{i=1}^{n} \frac{w_{i+n}}{1 + e^{-(w_i T + b_i)}} - \sum_{i=1}^{n} \frac{w_{i+n}}{1 + e^{-b_i}} = 0 \tag{47}$$

and it is now possible to express one chosen parameter as a combination of the other ones, for instance, the last output weight $w_{2n}$:

$$w_{2n} = -\frac{\sum_{i=1}^{n-1} w_{i+n}\{[1/(1 + e^{-(w_i T + b_i)})] - [1/(1 + e^{-b_i})]\}}{[1/(1 + e^{-(w_n T + b_n)})] - [1/(1 + e^{-b_n})]} \tag{48}$$

thus reducing the dimension of the parameter space. Several methods based on different heuristical algorithms have also been tested, such as random adaptive search and simulated annealing, but we will focus here on the results given by the GA.

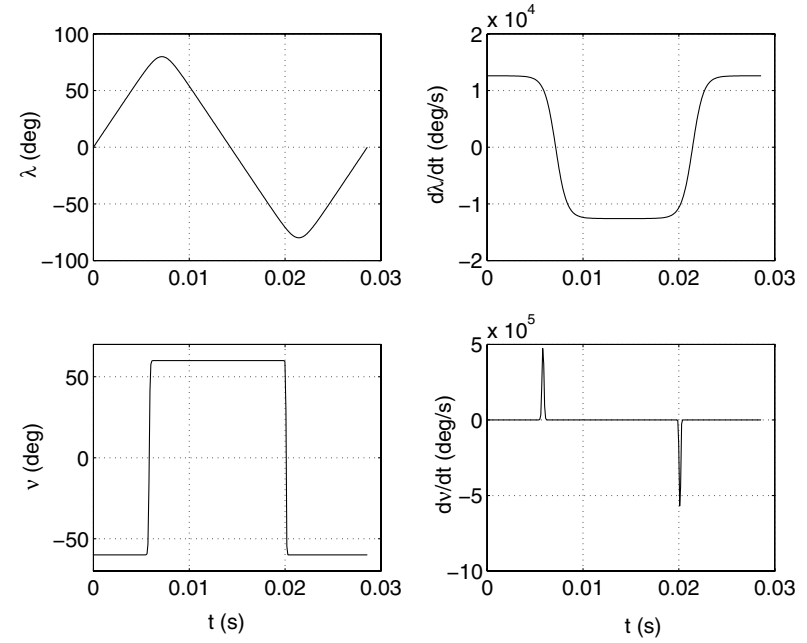


**a) Inputs $\lambda, \nu$**

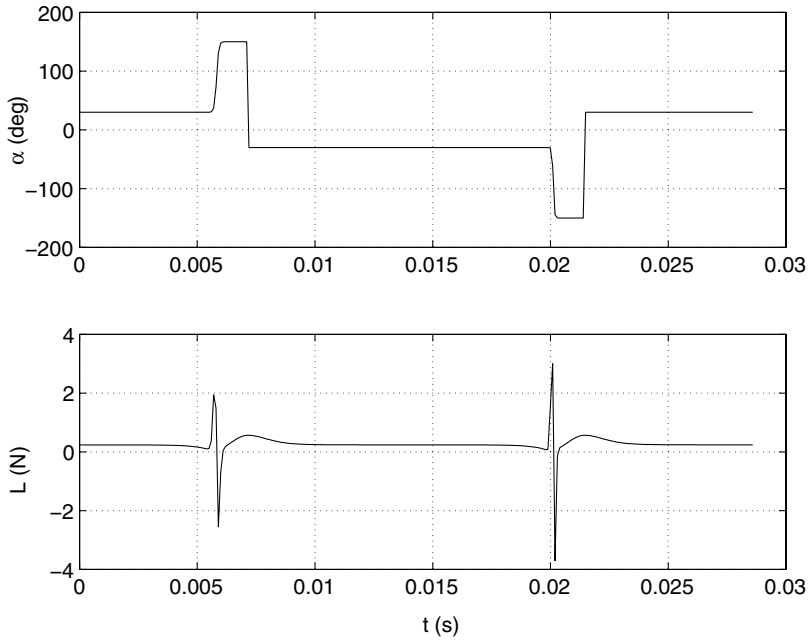


**b) Outputs $\alpha, L$**

**Fig. 17 Optimization of $v$ while minimizing quadratic horizontal velocity $u^2$.**

## Results

A reference case was defined using standard functions for the flapping angle $\lambda_r(t)$ and the rotation angle $\nu_r(t)$, respectively, defined as (values in degrees)

$$\nu_r(t) = 60 \tanh\left(10 \cos \frac{2\pi t}{35}\right) \tag{49}$$

$$\lambda_r(t) = 80 \int_0^t \tanh\left(4 \cos \frac{2\pi u}{35}\right) \mathrm{d}u \tag{50}$$

Those functions and their respective time derivatives are represented in Fig. 14a, and the corresponding local aerodynamic angle of attack $\alpha$ and lift $L$ in Fig. 14b. Those functions were arbitrarily chosen after studying the kinematics of many flying animals in nature. The corresponding mean lift over a period is $\bar{L}_r = 0.1994$ N, and the stroke plane is horizontal ($\xi = \pi/2$; see Fig. 2).

### Rotation Angle

In a first series of calculations the rotation angle $\nu(t)$ was optimized, $\lambda$ being equal to $\lambda_r$. The result is shown in Fig. 15 for a horizontal stroke plane. The mean lift is $|\bar{L}| = 0.2649$ N, which represents a gain of about 33% in comparison with the reference case. The optimal function shape is close to the standard one, but it is very interesting to notice how these results fit with previously observed mechanisms: the optimal function shows a phase lead (+18.44 deg) with respect to the reference one (which was not dephased). This corroborates the fact that an advanced rotation can bring an extra lift, in contrast to symmetrical kinematics, as observed with experimental devices such as *Robofly* [7]. Another significative point is that this phase lead did not appear explicitly within the model of the function:

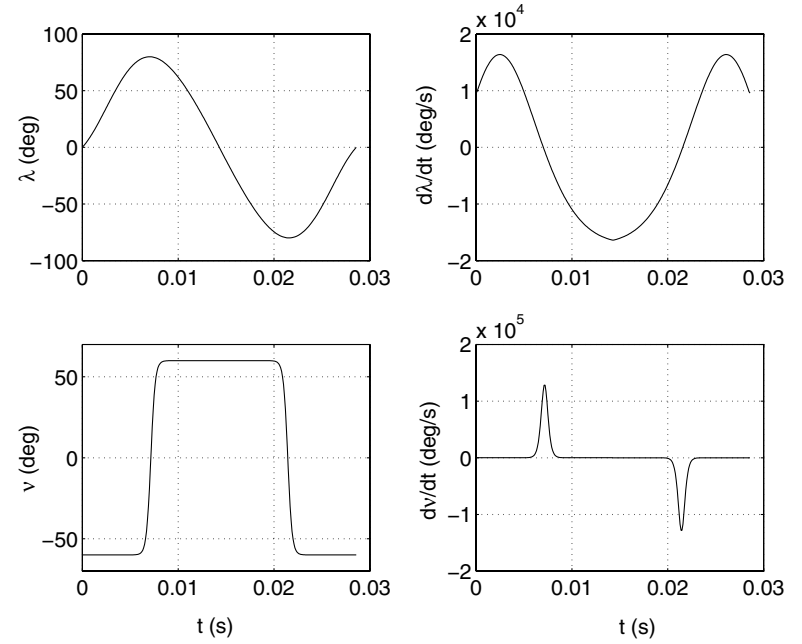


**a) Inputs $\lambda, \nu$**

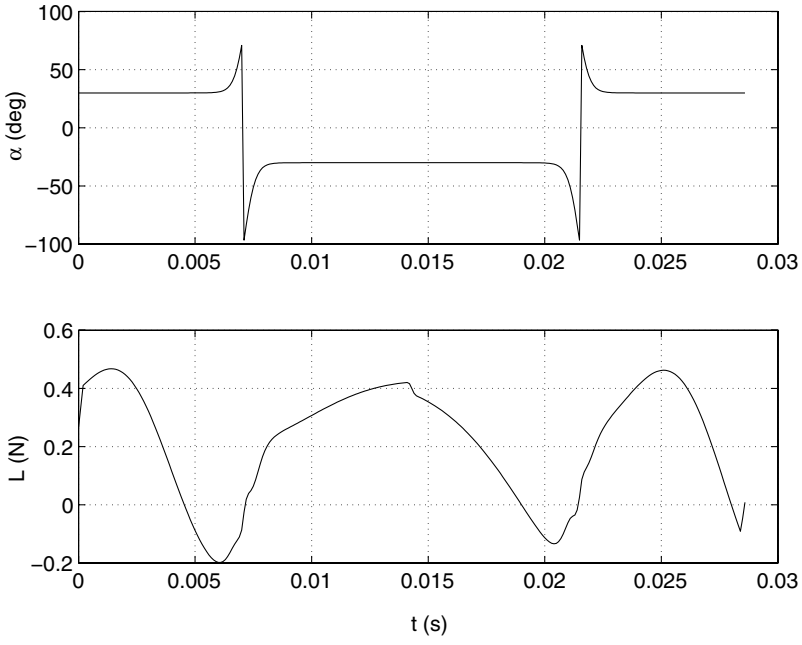


**b) Outputs $\alpha, L$**

**Fig. 18 Optimization of λ while limiting $\dot{\lambda}_{max}$.**

the weights of the neural network are indeed not directly interpretable in terms of physical components of the output function such as amplitude or phase.

The same method was applied for an inclined stroke plane: $\xi = 45$ deg. This configuration is also widely used by the natural flyers, in particular by the *Odonates* [20]. The results are shown in Fig. 16. This time, the rotation angle is asymmetrical ($\nu_{max} \neq -\nu_{min}$), a feature also present in nature when the stroke plane is inclined. But this optimal shape features a large rotation amplitude of the wing (it performs $3/4$ of a complete rotation around its axis; see Fig. 16c) that is not found in animal flight, because of some inherent articular limitations.

The efficiency of this particular wing motion scheme could be corroborated by means of the test facilities involved in the REMANTA project. In that case a water tunnel and a water tank in which hydrodynamic forces measurements will be performed on a mechanical wing using various kinematics [21].

It is also interesting to consider the horizontal displacements of the MAV while hovering. Large-amplitude oscillations in the horizontal plane would indeed greatly impede objectives such as video or infrared acquisition. This is why another set of computations has been done with a secondary criterion corresponding to a minimal quadratic speed along the horizontal forward $\boldsymbol{x}_0$-axis (because the movements of both wings are symmetrical, no displacement is expected along the lateral axis).

The GA which was used here does not take explicitly into account several criteria; this is why the proposed method is to incorporate the secondary criterion by adding a penalty term to $J$:

$$\tilde{J} = \alpha_u J - e^{\beta_u u^2} \tag{51}$$

$\alpha_u$ and $\beta_u$ are weighting coefficients, which were, respectively, set after a few iterations to $\alpha_u = 1$ and $\beta_u = 0.1$ to have a correct balancing between the two components. The results of the

optimization of $\tilde{J}$ are shown in Fig. 17. The mean lift is $|\bar{L}| = 0.2619$ N, and the optimal rotation angle is very close to the first case (Fig. 15).

#### Flapping Angle

The genetic algorithm did not give acceptable results for the optimization of $\lambda$ using the standard criterion: the optimal function presented very sharp variations and, besides the fact that the corresponding flapping speed $\dot{\lambda}$ would have been unreachable by any physical actuator, the inner nonlinearities of the model generated too many singular points during the simulation. The criterion was then modified to explicitly limit the peaks of $\dot{\lambda}$ by addition of a penalty term, as it was done previously to limit the quadratic horizontal velocity:

$$\tilde{J} = \alpha_\lambda J - e^{\beta_\lambda |\dot{\lambda}|_{\max}} \tag{52}$$

Figure 18 shows the result obtained for $\alpha_\lambda = 1$ and $\beta_\lambda = 0.1$. This time the optimal function shape is much smoother, and close to a sinusoid. The lift gain is quite important: $|\bar{L}| = 0.2794$ N, or $+40\%$, which suggests that this function shape might be preferred over the triangular reference one $\lambda_r$ in further simulations. This type of kinematics would also be more convenient to implement on a real MAV, by using, for example, a steady oscillating resonant structure to drive the flapping.

## Conclusion and Further Work

A simulation model has been developed for a flapping-wing microair vehicle, which includes the specific aerodynamic effects for low-Reynolds number flapping flight. The first simulation results show very similar results to those obtained by some authors, in particular the lift gain brought by the rotation of the wing. A simplified model has also been written, which restrains the flight into a vertical plane (longitudinal flight) and allows the relation between the kinematics of the wing and the movements of the MAV to be written in analytical form, using nonlinear scalar functions. In a second part, the wing kinematics have been modeled using neural networks designed to reproduce the widest class of suitable function shapes. A genetic algorithm has then been used to find the optimal kinematics so as to maximize the mean lift and thus the available payload, without being trapped in the many local optima. The result shows close similarities to previously obtained experimental results, in particular the fact that a lead advance of $\nu$ (rotation) with respect to $\lambda$ (flapping) brings an extra lift. The mean lift was improved by 30 to 40% in comparison with a reference case. Because this model can simulate the 6-degrees of freedom motion of the MAV, a similar procedure could be used for longitudinal flight (e.g., to maximize the forward speed). The next step is the development of nonlinear control methods to stabilize and pilot the MAV in closed loop.

## References


[1] Descatoire, F., Moing, T. L., Bruyant, F., and Morlière, A., "PRF REMANTA: Analyse de concepts de microdrones á ailes vibrantes," ONERA/DPRS—Ressources générales, Rapport technique 7/06779, March 2003.

[2] Weis-Fogh, T., "Energetics of Hovering Flight in Hummingbirds and in Drosophila," *Journal of Experimental Biology*, Vol. 56, No. 1, 1972, pp. 79–104.

[3] Weis-Fogh, T., "Quick Estimates of Flight Fitness in Hovering Animals, Including Novel Mechanisms for Lift Production," *Journal of Experimental Biology*, Vol. 59, No. 1, 1973, pp. 169–230.

[4] Ellington, C., "The Aerodynamics of Hovering Insect Flight," *Philosophical Transactions of the Royal Society of London Series B, Biological Sciences*, Vol. 305, No. 1122, Feb. 1984, pp. 1–181.

[5] Żbikowski, R., "On Aerodynamic Modelling of an Insect-Like Flapping Wing in Hover for Micro Air Vehicles," *Philosophical Transactions. Series A, Mathematical, Physical, and Engineering Sciences*, Vol. 360, No. 1791, 2002, pp. 273–290.

[6] Norberg, U., "The Cost of Hovering and Forward Flight in a Nectar Feeding Bat, *Glossophaga Soricina*, Estimated from Aerodynamic Theory," *Journal of Experimental Biology*, Vol. 182, No. 1, 1993, pp. 207–227.

[7] Dickinson, M., Lehmann, F.-O., and Sane, S., "Wing Rotation and the Aerodynamic Basis of Insect Flight," *Science*, Vol. 284, June 1999, pp. 1954–1960.

[8] Rakotomamonjy, T., Le Moing, T., and Ouladsine, M., "Simulation Model of a Flapping-Wing Micro Air Vehicle," *First European Micro Air Vehicle Conference and Flight Competition (EMAV)*, Deutsche Gesellschaft für Ortung und Navigation, Braunschweig, July 2004.

[9] Sane, S., and Dickinson, M., "The Aerodynamic Effects of Wing Rotation and a Revised Quasi-Steady Model of Flapping Flight," *Journal of Experimental Biology*, Vol. 205, No. 8, 2002, pp. 1087–1096.

[10] Llibre, M., *Modélisation et Commande des Systèmes Mécaniques Articulés*, Cours Supaéro, Toulouse, France, June 2002.

[11] Dickinson, M., and Götz, K., "Unsteady Aerodynamic Performance of Model Wings at Low Reynolds Numbers," *Journal of Experimental Biology*, Vol. 174, No. 1, 1993, pp. 45–64.

[12] Norberg, U., *Vertebrate Flight*, Vol. 27, Zoophysiology, Springer–Verlag, Berlin Heidelberg, 1990.

[13] Fung, Y., *An Introduction to the Theory of Aeroelasticity*, Dover, New York, 1993.

[14] Walker, J., "Rotational Lift: Something Different or More of the Same?," *Journal of Experimental Biology*, Vol. 205, No. 24, 2002, pp. 3783–3792.

[15] Taylor, G., "Mechanics and Aerodynamics of Insect Flight Control," *Biological Reviews of the Cambridge Philosophical Society*, Vol. 76, No. 4, 2001, pp. 449–471.

[16] Kurtulus, D., Farcy, A., and Alemdaroglu, N., "Unsteady Aerodynamics of Flapping Airfoil in Hovering Flight at Low Reynolds Numbers," AIAA Paper 2005-1356Jan. 2005.

[17] Rakotomamonjy, T., Le Moing, T., and Ouladsine, M., "Développement d'un Modèle de Simulation d'un Microdrone à Ailes Vibrantes," *Conférence Internationale Francophone d'Automatique*, Ecole Centrale de Lille, Douz, Nov. 2004.

[18] Rakotomamonjy, T., Le Moing, T., and Ouladsine, M., "Kinematics Optimization for a Flapping-Wing Micro Air Vehicle," *16th International Federation of Automatic Control World Congress*, Elsevier, July 2005.

[19] Ouladsine, M., Bicking, F., and Bloch, G., "Identification of Constrained Dynamic-Systems by Genetic Type Algorithm," *Proceedings of the Artificial Intelligence in Real Time Control*, Pergamon, 1995.

[20] Wakeling, J., and Ellington, C., "Dragonfly Flight. 2. Velocities, Accelerations and Kinematics of Flapping Flight," *Journal of Experimental Biology*, Vol. 200, No. 3, 1997, pp. 557–582.

[21] Luc-Bouhali, A., and Choy, P., "Progress of the REMANTA Project on MAV with Flapping Wings and of the International Universities Mini UAV Competition," *First European Micro Air Vehicle Conference and Flight Competition (EMAV)*, Deutsche Gesellschaft für Ortung und Navigation, Braunschweig, July 2004.